Optimizing the corrosion resistance of protective coatings in mechanical equipment through polymer materials



Digby D. Macdonald¹

¹Departments of Nuclear Engineering and Materials Science and Engineering, University of California at Berkeley, Berkeley, California, 94720, United States of America

*Corresponding Author: macdonald@berkeley.edu

Received: 28/01/2023 Revised: 11/01/2024 Accepted: 02/03/2025 Published: 26/10/2025

©2025 The Author(s). This is an open access article under the CC BY license https://creativecommons.org/licenses/by/4.0/

Abstract: To address corrosion issues in chemical machinery and equipment, ensuring the safety and reliability of chemical plant operations, this paper presents an effective anti-corrosion solution using "polymeric chemical materials" as an application example. Polypyrrole (PPv) offers advantages such as easy synthesis, film-forming capability, high conductivity, excellent stability, and environmental friendliness. By coating various metal and non-metal substrates with vanadium pentoxide (V_2O_5) sol-gel and employing the VPP method, PPy/V_2O_5 composite materials are synthesized under ambient temperature and pressure conditions. Structural characterization was performed using X-ray energy dispersive spectroscopy (XEDS) and Fourier transform infrared spectroscopy (FTIR). Corrosion resistance was evaluated through gravimetric weight loss and electrochemical testing. Results demonstrated no significant corrosion on the 1:1 PPy/V₂O₅ composite coating surface after 60 days of immersion in a 3.5 wt% NaCl solution. When characterizing the corrosion inhibition effect of the inhibitor through weight loss experiments and electrochemical testing, the incorporation of nano-SiO₂ enhanced the film's corrosion resistance by strengthening the mechanical shielding effect of the coating and suppressing charge transfer during the corrosion reaction, thereby effectively protecting mechanical equipment.

Keywords: polypyrrole, X-ray energy dispersive spectroscopy, composite materials, electrochemical testing, gravimetric method, corrosion protection

1 | Introduction

Polymer polymerization coatings have found extensive applications in anti-corrosion, anti-fouling, and anti-icing coating fields due to their outstanding properties [1, 2]. Traditional coatings based on thermosetting materials are difficult to repair once damaged or degraded, posing serious safety hazards to equipment production [3]. With the advancement of science and technology, new requirements for protective coating materials have emerged, emphasizing long service life and ease of repair [4]. Organic polymeric protective coatings represent one of the most widely applied and effective corrosion prevention strategies for engineering and analytical equipment [5]. Among these, polyurethanes are the most prevalent polymeric materials, characterized by their structure linked through chemical bonds such as urethane and urease bonds [6]. At the molecular chain segment

level, their most distinctive feature is the presence of numerous, repeatedly occurring urethane segments within the polymer backbone. As a pollution-free and safe material, water-based polyurethane aligns with green development principles and represents a key direction in the development of environmentally friendly coatings [7, 8].

Xu et al. [9] reported subjecting three polyester polymer coatings to two years of natural exposure in Qionghai, Shenyang, and Turpan, China. They observed that environmental factors—high temperature and humidity, high irradiance, and high salinity—exerted synergistic effects accelerating coating degradation. Thuy [10] developed a polymeric polyurea coating by incorporating 3% nano-clay additives into a polyaspartic ester and isocyanate curing system. This coating passed mechanical and chemical performance tests, showing no peeling, bubbling, or gloss loss after 500 hours of UV exposure, demonstrating excellent mechanical, chemical, and weather resistance. Rossi et al. [11] conducted an in-depth analysis of the weathering mechanism of novel polyurethane powder coatings. The coatings demonstrated strong photochemical performance in accelerated condensation cycle tests, with chemical corrosion resistance varying with solvent exposure time, making them highly valuable for mechanical equipment protection. Silbert et al. [12] developed a polymeric protective coating by crosslinking polyurethane with 1,4-cyclohexanedicarboxaldehyde and 2,5-dimethylfuran (DFF). This coating passed spectral, thermal, and standard ASTM coating characterization tests, exhibiting high hardness and excellent solvent resistance. Zomorodian et al. [13] developed a polymer composite coating containing polyetherimide, several diethylenetriamines, and hydroxyapatite. Electrochemical impedance spectroscopy and scanning electron microscopy validated the coating's ability to slow the corrosion rate of AZ31 magnesium alloy.

Potočić Matković et al. [14] conducted an in-depth exploration of the application value of protective coatings on knitted fabrics. Researchers designed multiple coated knitted fabrics for protective clothing, which were exposed outdoors for three months under extreme weather conditions. Test samples exhibited reduced thermal resistance due to partial degradation of the polyurethane layer, providing a basis for improving the thermal protection of coatings. In the field of polymeric polymer coatings, coatings have already demonstrated resistance to organic acid media, dichloromethane, and high-salinity water environments, providing insights for future development of polymer-enhanced protective coating technologies [15, 16]. Concurrently, integrating advanced detection methods enables real-time identification of coating defects during application, reducing maintenance intensity and enhancing coating protective quality [17, 18].

This paper conducts a theoretical analysis of corrosion-protective coatings for mechanical equipment, focusing on PPy/V₂O₅ polymer composites as the research subject and establishing experiments to evaluate their anti-corrosion performance on machinery. First, a vanadium pentoxide (V₂O₅) aqueous sol was used to coat various metal and non-metal substrates. Subsequently, PPy/V₂O₅ composites were synthesized at ambient temperature and pressure using the VPP method. The structure of the PPy/V₂O₅ composite was characterized using scanning electron microscopy (SEM), energy-dispersive X-ray spectroscopy (EDX), Fourier transform infrared spectroscopy (FTIR), and infrared spectroscopy analysis. Finally, the corrosion-resistant performance of the composite material was evaluated through gravimetric weight loss testing, electrochemical testing, and adsorption isotherm analysis.

2 | Optimization of corrosion resistance performance of polymer protective coatings in mechanical equipment

2.1 | Common types of corrosion in mechanical equipment

2.1.1 | Chemical corrosion

Chemical corrosion refers to material damage directly caused by chemical reactions, including the direct chemical reactions of acids, alkalis, and salts with metals. Such reactions lead to gradual degradation of equipment materials without the involvement of electric current, resulting in localized loss. Corrosion causes equipment walls to thin and strength to diminish, potentially triggering leaks or even explosions. This corrosion phenomenon is commonly observed in tanks and pipelines storing acidic or alkaline chemicals.

Taking acid corrosion as an example, sulfuric acid (H_2SO_4) and hydrochloric acid (HCl) are common corrosive media in chemical production. When these acids come into contact with the surface of metal equipment, they react rapidly to form corresponding metal salts and hydrogen gas. For instance, sulfuric acid reacting with iron sheet produces ferrous sulfate $(FeSO_4)$ and hydrogen gas (H_2) , as shown in the chemical equation: $Fe + H_2SO_4 \rightarrow FeSO_4 + H_2\uparrow$. This reaction not only consumes the equipment material but also poses significant safety risks due to the generated hydrogen gas. In alkaline corrosion scenarios, strong alkalis like sodium hydroxide (NaOH) similarly react with metals—particularly reactive metals such as aluminum and zinc—forming corresponding metal hydroxides and hydrogen gas. This process also leads to material degradation and diminished structural integrity of equipment.

2.1.2 | Electrochemical Corrosion

Electrochemical corrosion occurs due to electron transfer in electrolytes, commonly observed when metals contact electrolytes (such as salt solutions in water). During this corrosion process, the metal surface dissolves as an anode, while a reduction reaction occurs at another location in the same electrolyte (the cathode). For example, the corrosion reaction of iron in aqueous solutions containing chloride ions (Cl⁻) is: Fe \rightarrow Fe²⁺ + 2e⁻. Electrochemical corrosion frequently leads to pitting corrosion and cracks forming near waterlines or at minute defects in equipment. Damage begins microscopically and accumulates over time, eventually expanding into macroscopic failure. For instance, stainless steel is highly susceptible to pitting corrosion in chloride-containing environments. Although stainless steel surfaces typically form a stable protective chromium oxide layer, chloride ions can penetrate this layer and create microscopic anodic areas on the metal surface, accelerating localized corrosion. Such pitting corrosion is difficult to detect early. Once formed, it progresses extremely rapidly and may ultimately lead to equipment perforation.

2.1.3 | Biological corrosion

Biocorrosion is a corrosion process caused by the life activities of microorganisms (including bacteria, fungi, algae, etc.), commonly occurring in parts of chemical machinery that come into contact with water. Bacteria such as sulfate-reducing bacteria (SRB) can induce metal corrosion by reducing sulfate ions (SO₄²⁻) into hydrogen sulfide (H₂S). The chemical reaction equation is: $SO_4^{2-} + 2H_2O + 2O_2 \rightarrow 2H_2S + 2HCO_3^-$. Biocorrosion not only leads to material loss but may also produce toxic gases and accelerate metal corrosion rates, posing threats to chemical production safety and personnel safety.

2.2 | Corrosion resistance properties of polymer chemical materials

Polymer materials possess characteristics such as structural stability and strong corrosion resistance. Relevant personnel should fully leverage and utilize these properties when applying them to the design of chemical machinery and equipment. By employing polymer materials in the scientific fabrication of chemical machinery, the risk of leakage in manufactured equipment such as metering tanks and valves can be reduced. Consequently, polymer materials are hailed as the "optimal anti-corrosion materials for chemical applications." For polymeric materials, their high chemical inertness protects the polyvinyl chloride (PVC) backbone, preventing varying degrees of chemical damage to this main chain.

Additionally, the fundamental cause of varying degrees of corrosion in certain chemical machinery equipment lies in the proliferation and erosion of substantial microbial populations within these systems. The emergence and application of polymeric materials disrupt the microbial breeding environment, thereby reducing the risk of corrosion in chemical machinery equipment. After undergoing a series of chemical treatments with polymeric materials, the coating formed on the material's surface exhibits high corrosion resistance. This coating, an unsaturated polyester resin, displays S-148 aromatic characteristics. When this coating is immersed in a 70% sulfuric acid solution at room temperature for 2 hours, the surface gradually darkens, forming a thin blackened layer. However, no significant internal changes occur within the coating. This indicates that the 70% sulfuric acid solution only induces varying degrees of chemical reaction on the surface layer. Under infrared spectroscopy analysis, combined with X-ray photoelectron spectroscopy (XPS) for comprehensive examination of the main chain benzene rings, varying degrees of sulfonation were observed on these rings. By fully integrating sulfonic acid groups with the main chain benzene rings, the surface structure stability and density of the polymeric material are significantly enhanced. Simultaneously, the newly introduced sulfonic acid groups exhibit high corrosion resistance and demonstrate strong attack on sulfuric acid. Leveraging steric hindrance effects, they effectively protect the primary structures within chemical machinery and equipment, preventing substantial sulfuric acid penetration into the equipment.

2.3 | Optimizing the corrosion resistance of polypyrrole in mechanical equipment

2.3.1 | Mechanical shielding effect

The primary corrosion protection of conventional organic coatings on metals stems from mechanical shielding. Conductive polymer PPy forms a dense, low-porosity coating with excellent adhesion on the metal surface, preventing oxidizing agents from reaching the metal substrate and thus providing a barrier. The lower the permeability of the conductive polymer layer, the slower the migration rates of ions, oxygen, and water, resulting in superior corrosion resistance. When evaluating the corrosion protection efficacy of electrochemically deposited polypyrrole (PPy) on Fe, it was observed that only when the coating thickness exceeded $1\mu m$ did the PPy coating exhibit significant corrosion-inhibiting effects.

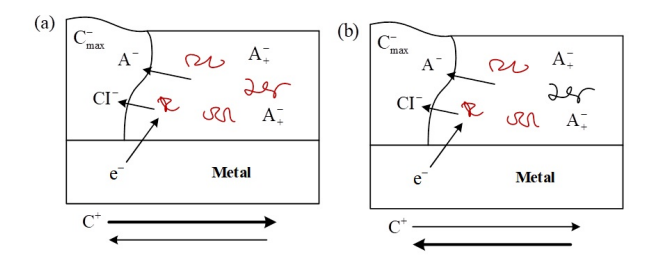
2.3.2 | Mechanism of corrosion inhibitors

When the PPy film on a metal surface is immersed in a corrosive environment, PPy "dedoping" occurs, releasing anions with corrosion-inhibiting capabilities. These anions accumulate at the interface between the metal and PPy the film. Some of the released dopant ions react with external cations to form insoluble protective

D. D. MACDONALD 25

compounds, achieving a corrosion-inhibiting effect. Further studies indicate that when the longitudinal edge of the coating cross-section contacts the electrolyte, not only anion release occurs but also cation injection. The ion exchange between the solution and the coating depends on the radius of the doped anions. Polymer coatings prepared from PPy doped with different types of anions exhibit varying degrees of corrosion inhibition capability, significantly affecting long-term corrosion protection performance.

When corrosion occurs, metals act as anodes to undergo oxidation reactions, while polymers act as cathodes to undergo reduction reactions. The reaction process involves electron transfer and ion migration in the metal substrate, PPy coating, and the external corrosive environment (electrolyte), as shown in Figure 1. In Figure 1(a), when there are large cations in the electrolyte, the doped anions are released preferentially. At the same time, the chloride ions contained in the electrolyte enter the coating and continuously exchange with the anions doped in the polymer. When the chloride ions entering the coating reach the metal surface, it will cause pitting corrosion on the metal surface and accelerate the corrosion rate. Therefore, large-volume anions are usually selected as PPy dopants. By slowing down the exchange process between anions and anions and controlling the release rate of doped anions, a long-lasting anti-corrosion effect can be achieved. In Figure 1(b), when there are small-sized cations in the electrolyte, while the doped anions are released in the coating, small-sized cations also enter. Cations entering will neutralize some anions, prevent the release of doped anions, and at the same time, cations move between polymer chains in a jumping transfer manner, triggering the reduction of the polymer and promoting the entry of other cations, accelerating the failure of the coating. Therefore, when studying the corrosion inhibition mechanism, the corrosion environment of the coating and the composition of the electrolyte should be fully considered.



 ${
m FIGURE}\ 1$ Migration of chloride ions and cations and release of anion of corrosion inhibitor

2.3.3 | Mechanism of electrochemical interface migration

Conventional organic coatings cannot transmit electrons, causing both anodic and cathodic reactions to occur at the metal-coating interface. These reactions generate OH^- ions, leading to coating degradation and delamination. However, the conductive PPy coating enables electron transmission, shifting the corrosion reaction interface. Simultaneously, a concentration gradient of oxygen along the polymer layer causes the cathodic reaction to occur at the coating/solution interface, while the anodic reaction remains at the coating/metal interface. This prevents the accumulation of large amounts of OH^- at the metal surface, inhibits the rise in pH at the metal surface, and promotes the formation of stable oxides on the metal surface. Consequently, both the corrosion rate and the coating delamination rate are reduced, as illustrated in Figure 2.

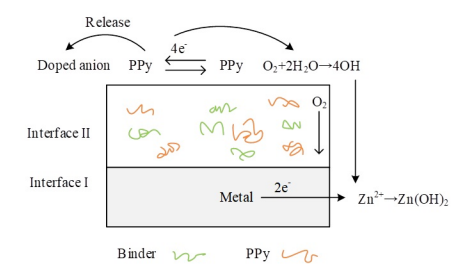


FIGURE 2 Schematic explanation of interface migration

3 | Experimental evaluation of corrosion resistance properties of pyrrole nanocomposite coatings

3.1 | Preparation of experimental materials

3.1.1 | Reagents and instruments

The main reagents and instruments used in the experiments of this chapter are listed in Tables 1 and 2.

TABLE 1 Experimental reagents

Reagent	Rank
Pyrrole	AR
Acetone	AR
Absolute ethyl alcohol	AR
Toluene-p-sulfonic acid	AR
Deionized water	-
High purity nitrogen	99.999%
Ammonium metavanadate	AR
Sodium chloride	AR
Magnesium sheet	99.7%
Nickel sheet	99.7%
Zine plate	99.5%
Polyethylene terephthalate plate (PET)	-
PMMA sheet (PMMA)	-
Polyimide base (PI)	-
Polyvinyl chloride panel (PVC)	-

TABLE 2 Experimental instruments

Instrument name	Model
Electrochemical workstation	Autolab 302N
Scanning electron microscope	SU-70
Ultrasonic cleaner	KQ5200DE
Electronic balance	AL104
Electric thermal constant temperature fan drying chamber	DHG-9140A
Vacuum drying oven	DZF-6020
Suction pipet	5mL
Transfer liquid gun	100,100 μL
Thermostat water bath	DK-450B
x X	Bruker-axs
Fourier infrared spectrometer	Nicoet isl0
Step pyramids	ET150
Saturated calomel electrode	Type 232
Dual-electrical four-probe tester	RTS-9 type
Platinum sheet electrode	Type 213
Waterproof abrasive paper	A275 model

3.1.2 | Material preprocessing

Pyrrole should be stored in a -20° C refrigerator protected from light. Prior to use, perform a second distillation under nitrogen atmosphere.

Surface pretreatment of pure magnesium sheets (15×15 mm): Sequentially polish the surface using water-resistant sandpaper ranging from 800 to 3000 grit until the magnesium sheet achieves a mirror-like finish. Subsequently, immerse the prepared samples in deionized water and sonicate for 10 minutes. Transfer to analytical-grade anhydrous ethanol and sonicate for another 10 minutes. Finally, return to deionized water and sonicate for a further 10 minutes. Dry using a bulb syringe and store in a glass desiccator for later use.

Nickel plate (15×15mm) surface pretreatment method is similar to the above process. To prevent oxidation during deionized water treatment, polishing and ultrasonic cleaning are performed using deionized solution.

Zinc plate (15×30mm) surface pretreatment: The surface is sequentially polished with 800-3000 grit wet sandpaper to achieve a smooth mirror finish. Subsequently, the samples are immersed in deionized water and sonicated for 10 minutes, then transferred to analytical-grade anhydrous ethanol for another 10 minutes of sonication. Finally, they are placed back in deionized water for a final 10-minute sonication cycle. After drying with a bulb syringe, the samples are stored in a glass desiccator for later use.

Polyethylene terephthalate (PET) (10×10 mm) surface pretreatment: Immerse transparent samples in deionized water and sonicate for 10 minutes. Transfer to analytical-grade anhydrous ethanol and sonicate for

10 minutes. Finally, place in deionized water and sonicate for 10 minutes. Dry using a bulb syringe and store in a glass desiccator for later use.

Poly(methyl methacrylate) (PMMA) (10×10mm) surface pretreatment: Immerse transparent samples in deionized water and sonicate for 10 minutes. Transfer to analytical-grade anhydrous ethanol and sonicate for 10 minutes. Finally, place in deionized water and sonicate for 10 minutes. Dry using a bulb syringe and store in a glass desiccator for later use.

Polyimide (PI) (10×10 mm) Surface Pretreatment: Immerse the brown translucent sample in deionized water and sonicate for 10 min. Transfer to analytical-grade anhydrous ethanol and sonicate for 10 min. Finally, place in deionized water and sonicate for 10 min. Dry using a bulb syringe and store in a glass desiccator for later use.

Polyvinyl Chloride (PVC) (10×10mm) Surface Pretreatment: Immerse the opaque white sample in deionized water and sonicate for 10 minutes. Transfer to analytical-grade anhydrous ethanol and sonicate for 10 minutes. Finally, place in deionized water and sonicate for 10 minutes. Dry using a bulb syringe and store in a glass desiccator for later use.

3.1.3 | Preparation of vanadium pentoxide aqueous sol

The preparation steps for Sol V_2O_5 in this experiment, as outlined in the overall reference literature, are as follows:

- (1) Solution Preparation. Prepare 10 mL of hydrochloric acid (1 mol/L); prepare hot water by adding water to a 200 mL beaker and heating to 80°C, then maintain temperature for later use.
- (2) Initial Grinding. Add ammonium metavanadate powder to the mortar while slowly adding 7-8 drops of deionized water to ensure thorough absorption. Grind until no lumps remain and a paste-like consistency is achieved. This process takes approximately 5 minutes.
- (3) Secondary Grinding. Thoroughly grind the ammonium metavanadate powder from fine particles to an extremely fine powder. Grind until no granularity is felt, continuing for 5 minutes until a paste-like consistency is achieved.
- (4) Thoroughly mix. Transfer the ammonium metavanadate ground to a slurry in the mortar to a 50 mL beaker. Add 10 mL of prepared hydrochloric acid (1 mol/L) and wash the ammonium metavanadate from the mortar into the beaker, bringing the total volume to 20 mL.
- (5) Thoroughly stir and decant the supernatant. Stir the liquid in the beaker vigorously until no white particles remain. Continuously add hot water at 80°C to the system while decanting the upper clear layer. Retain the brick-red colloid at the bottom and continue stirring until the colloid achieves satisfactory uniformity.
- (6) Volume expansion preservation. If the final solution volume is less than 40 ml, add hot water at 80° C to expand the volume. Suspension storage for 50–60 days yields V_2O_5 -nanometer wires with a high aspect ratio.

3.1.4 | Mild VPP Method Process Flow

The mild VPP method procedure is shown in Figure 3. The steps for depositing the PPy composite using the VPP method are:

(1) Add the Py monomer to a 50 ml wide-mouth bottle and maintain sealing for 30 minutes to form a saturated vapor pressure of the Py monomer. Simultaneously, coat the magnesium substrate with the

previously stored V_2O_5 aqueous sol-gel oxidant.

(2) Rapidly transfer the V_2O_5 -water-soluble-gel-coated sample into the prepared Py-monomer saturated vapor pressure atmosphere for deposition polymerization reaction over 12 hours.

(3) Remove the Mg-sheet and dry at room temperature; the entire reaction process occurs under ambient temperature and pressure. The pyrrole monomer added during the reaction was in excess, sufficient to completely react with the V_2O_5 aqueous sol. No significant corrosion was observed on the metal substrate after the reaction, indicating that the reaction between the V_2O_5 aqueous sol as the oxidant and the pyrrole gas-phase monomer took precedence over the reaction between the oxidant and the metal substrate.

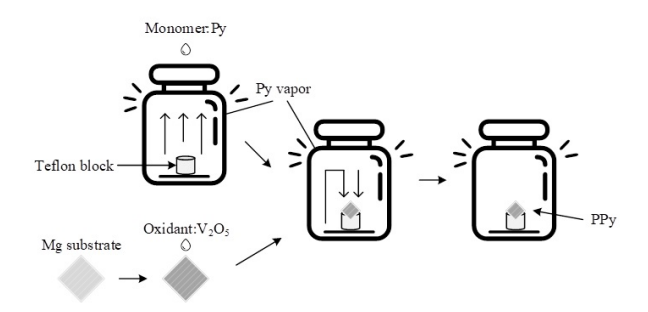


FIGURE 3 Schematic diagram of mild vpp method

3.2 | Characterization of the nanostructure of the PPy/V_2O_5 composite

3.2.1 | Scanning electron microscope (SEM)

Morphological analysis of $PPy/V_2O_5/Mg$ was conducted using a Hitachi SU-70 scanning electron microscope. Samples were pre-dried, and all specimens underwent platinum coating via ion sputtering to enhance conductivity. The initial acceleration voltage for SEM imaging was set at 5.0 kV, with adjustments made as necessary based on imaging conditions.

3.2.2 | X-ray energy dispersive spectroscopy (EDX)

Elemental composition analysis of the $PPy/V_2O_5/Mg$ sample was performed using the EDX mode of a Hitachi SU-70 scanning electron microscope. The sample was pre-dried and sputter-coated with platinum prior to imaging to enhance conductivity. The SEM acceleration voltage was set to 20.0 kV.

3.2.3 | Fourier transform infrared spectroscopy (FTIR)

The Nicoletis10 infrared spectrometer was employed to characterize the samples using the ATR mode, with air selected as the background. The spectral scan range was $500-4000 \text{ cm}^{-1}$; resolution: 8 cm^{-1} ; scan number: 16.

3.2.4 | Conductivity Study

Using an RTS-9 dual-electrode four-probe tester, the conductivity of multiple PPy/VO/Mg composite coating samples deposited and polymerized at room temperature was calculated through a two-step experimental process. Step 1: Measured film thickness at multiple locations on five samples using an ET150 step profiler. The measured path length was $500~\mu m$, with measurements taken at different positions. The final thickness for each sample was the average of all data points. Second, the resistivity of the five samples was measured using the RTS-9 four-probe conductivity tester (4PT, RTS-9, China). Measurements were taken at different sample points while applying four bidirectional voltages of 0.01, 0.10, 1.00, and 10.0 mV. The average value was taken as the resistivity of that sample. Finally, the conductivity was calculated from the resistivity.

3.3 | Evaluation of Corrosion Resistance

3.3.1 | Weightlessness Testing

The weight loss method experiment used bronze specimens measuring $30 \,\mathrm{mm} \times 10 \,\mathrm{mm} \times 1 \,\mathrm{mm}$. Specimens were segmentally polished using metallographic sandpaper (240 grit, 500 grit, 1000 grit, 2000 grit) until surfaces showed no visible scratches. They were rinsed with distilled water, followed by ultrasonic treatment with acetone and anhydrous ethanol. Weighing was performed with an accuracy of $\pm 0.1 \,\mathrm{mg}$. The etching solution comprised 50 mL of 3.5% NaCl solution supplemented with corrosion inhibitors (concentrations of 0.2%, 0.4%, 0.6%, 0.8%, 1.0%, and 1.2%). A 3.5% NaCl solution without corrosion inhibitor served as the blank control sample. Each test condition was replicated three times, with the average value recorded as the final result.

The entire microgravity experiment employed a static full-immersion method. Mechanical equipment sections were securely bound with nylon thread, suspended, and fully immersed in a corrosion solution containing corrosion inhibitors. After 7 days, the experiment concluded. The mechanical equipment sections were removed from the corrosion solution, immersed in a 5% nitric acid solution for approximately 15 seconds, and surface corrosion products were wiped off with an eraser. Following rinsing with distilled water, the sections were soaked in anhydrous ethanol, dried, and weighed.

Based on the specimen's mass loss, the corrosion rate C_R is calculated as

$$C_R = \frac{m_0 - m_1}{At}. (1)$$

Here, C_R is the corrosion rate $(g cm^{-2} \cdot h^{-1})$; m_0 and m_1 are the masses before and after corrosion (g); A is the exposed area of the specimen (cm^2) ; and t is the exposure time (h).

The corrosion inhibition efficiency, $\eta(\%)$, is calculated as

$$\eta(\%) = \frac{C_{R0} - C_R}{C_{R0}} \times 100. \tag{2}$$

Here, C_{R0} is the corrosion rate of bronze in uninhibited 3.5% NaCl (g cm⁻² h⁻¹), and C_R is the corrosion rate of bronze in 3.5% NaCl containing the inhibitor (same units).

Unless otherwise specified in subsequent experiments, 3.5% NaCl solution shall be uniformly used as the corrosion medium for weight loss experiments, with a uniform immersion duration of 7 days.

3.3.2 | Electrochemical testing method

The AC impedance method [19] involves exciting the system under test by applying a weak AC electrical signal to the test system, thereby obtaining the corresponding feedback current (or voltage) signal. From these signals, the electrode impedance or admittance can be determined. The advantages of the AC impedance method include minimal system interference; the ability to reflect multi-angle interface states, facilitating analysis of corrosion inhibition mechanisms; and a relatively simple data analysis process yielding reliable results. Its disadvantage lies in the complexity of impedance spectrum parameters, which can be difficult to interpret. The Nyquist plot is a commonly used electrochemical impedance spectrum, where the horizontal axis represents the real part of impedance and the vertical axis represents the imaginary part. Key characteristics of the Nyquist plot include: a semicircle in the high-frequency region representing charge transfer processes, and a straight line in the low-frequency region representing ion diffusion. The semi-major axis of the impedance semicircle represents the charge transfer resistance of the corrosion reaction. A longer semi-major axis indicates a more complex corrosion reaction, suggesting the coating effectively resists attack by corrosive ions and exhibits excellent corrosion resistance.

Electrochemical experiments were conducted using an electrochemical workstation (CHI350E), employing saturated calomel, platinum sheet, and bronze as the reference electrode, auxiliary electrode, and working electrode, respectively. The effective exposed area of the working electrode during testing was 1.0 cm². Tests were conducted at room temperature. Prior to sequential AC impedance and Tafel curve measurements, the working electrode was immersed in 3.5% NaCl solution containing a corrosion inhibitor for 30 minutes.

Tafel polarization curves were recorded over the potential range from -0.80 to +0.10 V at a scan rate of 1 mV s⁻¹. The corrosion inhibition efficiency, $\eta(\%)$, is calculated as

$$\eta(\%) = \frac{i_{\text{corr},0} - i_{\text{corr}}}{i_{\text{corr},0}} \times 100. \tag{3}$$

Here, $i_{\text{corr},0}$ is the corrosion current density of bronze in uninhibited 3.5% NaCl (A cm⁻²), and i_{corr} is the corrosion current density of bronze in 3.5% NaCl containing the inhibitor (same units).

The corrosion inhibition rate is calculated from the corrosion current density, enabling quantitative assessment of the inhibitor's effectiveness.

The slope of the polarization curve also reflects the difficulty of the corrosion reaction. A lower absolute value of the polarization curve slope indicates greater difficulty in the corrosion reaction at the electrode, resulting in weaker corrosion; conversely, a higher absolute value of the polarization curve slope indicates easier corrosion reaction, leading to stronger corrosion.

Electrochemical impedance spectroscopy (EIS) was performed over the frequency range 10^{-2} – 10^4 Hz with an AC perturbation amplitude of 10 mV. Data were analyzed and fitted using ZView, and the inhibition efficiency $\eta(\%)$ was calculated as

$$\eta(\%) = \frac{R_{\rm ct} - R_{\rm ct,0}}{R_{\rm ct}} \times 100.$$
(4)

Here, $R_{\rm ct,0}$ is the charge-transfer resistance of bronze in uninhibited 3.5% NaCl ($\Omega \cdot {\rm cm}^2$), and $R_{\rm ct}$ is the charge-transfer resistance of bronze in 3.5% NaCl containing the inhibitor at the specified concentration (same units).

3.3.3 | Adsorption isotherms

Adsorption thermodynamics aims to elucidate the mechanism of corrosion inhibitors by establishing isothermal adsorption models, quantifying the relationship between adsorption thickness on metal surfaces and inhibitor solution concentration, and calculating physicochemical parameters such as adsorption equilibrium constants, Gibbs free energy, or other relevant physicochemical parameters. These parameters are then utilized to determine the mechanism of inhibitor action. Common adsorption isotherm equations include Langmuir, Temkin, Freundlich, and Flory-Huggins models. Chitosan-based corrosion inhibitors belong to the adsorption-type category, where their inhibition efficiency (η) approximates the surface coverage (θ) of the sample. The coverage data is then fitted against concentration to derive the adsorption isotherm model and thermodynamic adsorption parameters, with the calculation formula presented in Eq. (5).

$$0 = \eta. (5)$$

Among these, η represents the corrosion inhibition rate, and θ denotes the surface coverage. The Gibbs adsorption free energy ΔG_{ads}^0 is calculated using the formula shown in Eq. (6):

$$\Delta G_{ads}^0 = -RT \ln(10^3 K_{ads}). \tag{6}$$

Here, R is the gas constant with a value of $8.314 \text{ J} \cdot \text{K}^{-1} \cdot \text{mol}^{-1}$ and T is the absolute temperature (K).

3.4 | Findings and discussion

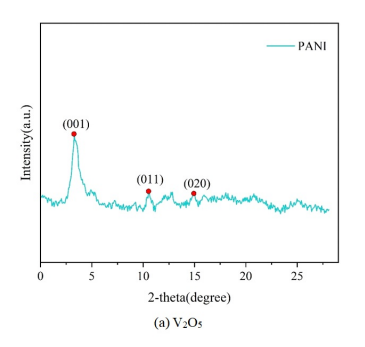
3.4.1 | X-ray diffraction spectral analysis

Figure 4 shows the XRD patterns of V2O5, VPP, pure Mg, V2O5/Mg with different contents and PPy/V2O5/Mg coatings. As can be seen from Figure 4(a), the diffraction peaks at 8.2°, 14.8°, and 18.5° correspond to the (001), (011), and (020) crystal planes of V2O5, respectively. The lower crystallinity is due to the repetition of the benzene and quinone rings on the chain. For PPy, the diffraction peak around 2θ =20° should be (002), which is the main peak of the sample, indicating that it is mainly composed of two-dimensional nanosheets with a high degree of exfoliation. After the combination of PPy/V2O5 and Mg, compared with the Mg coating, the V2O5/Mg and PPy/V2O5/Mg coatings both showed the (022) crystal plane diffraction peak of polyaniline at 2θ =29.9°. The diffraction peak of the PPy/V2O5/Mg composite coating gradually shifts to the left at around 20°. Moreover, the PPy/V2O5/Mg composite coating shows a wide peak near 2 θ =20°, indicating that the composite coating is a typical semi-crystalline/amorphous material.

3.4.2 | Fourier transform infrared spectroscopy analysis

Figure 5 shows the infrared spectra of V_2O_5 , VPP, pure Mg, and coatings with varying contents of V_2O_5/Mg and $PPy/V_2O_5/Mg$. As shown in Figure 5(a), the peak at 1677 cm⁻¹ corresponds to the -C=O stretching vibration in the NH-COO⁻ group of polyurethane, while the characteristic isocyanate peak at 2260 cm⁻¹ has disappeared. The peaks at 2915 cm⁻¹ and 2868 cm⁻¹ correspond to the stretching vibrations of methyl and methylene groups, respectively. The characteristic absorption peak of C-O-C appears near 1083 cm⁻¹. The urea group (-NHCON⁻) absorption peak at 1447 cm⁻¹ indicates the reaction between -NH₂ and -NCO, confirming

the successful preparation of polyurethane. Comparing Mg, V_2O_5 , and V_2O_5/Mg , the V_2O_5/Mg coating exhibits a -NH⁺ bending vibration absorption peak at 1152 cm⁻¹ with increasing polyaniline content, alongside C=C and C=O stretching vibration peaks at 1485 cm⁻¹ and 1573 cm⁻¹ for the benzene ring. As shown in Figure 5(b), another band near 1653 cm⁻¹ corresponds to interlayer water molecules in the PPy/V₂O₅/Mg coating and adsorbed water molecules on the coating surface. The band at 1143 cm⁻¹ corresponds to the stretching vibration mode of C-F in VPP, indicating the successful deposition of VPP nanosheets onto the coating.



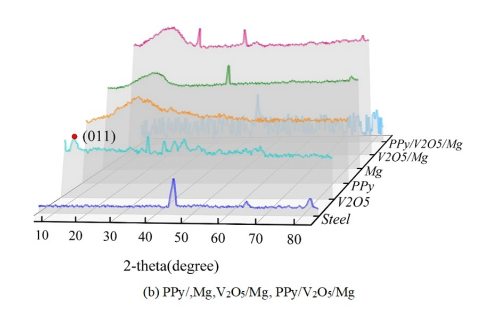


FIGURE 4 XRD pattern of the sample

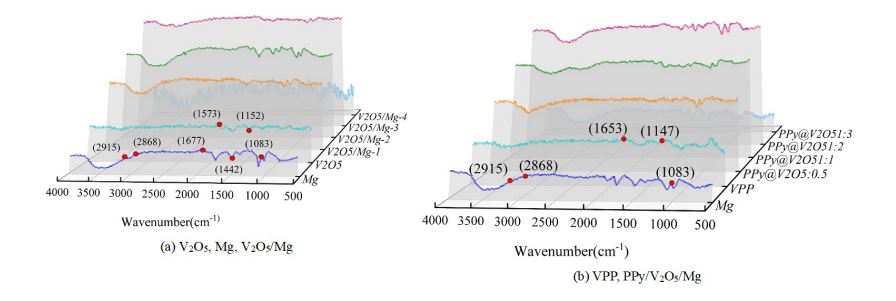


FIGURE 5 Infrared spectrum of sample

3.4.3 Ultraviolet-infrared spectral analysis of coatings

The UV spectrum of the sample is shown in Figure 6. As seen in Figure 6(a), the absorption peak at 295 nm corresponds to the $\pi - \pi^*$ absorption peak of the benzene ring in V₂O₅. With the addition of Mg, the absorption peak of polyaniline near 295 nm shifts toward 351 nm, exhibiting a red shift. This red shift becomes more pronounced as the polyaniline content increases. This phenomenon may result from enhanced conjugation between V₂O₅ and Mg, indicating the formation of bonds between these components. As shown in Figure 6(b), the added PPy exhibits UV absorption between 200–370 nm. Upon incorporation into the polyurethane, hydrogen bonding occurs between PPy and polyurethane, forming a substance with a crosslinked structure. This crosslinking enhances the absorption peak of the polyurethane coating.

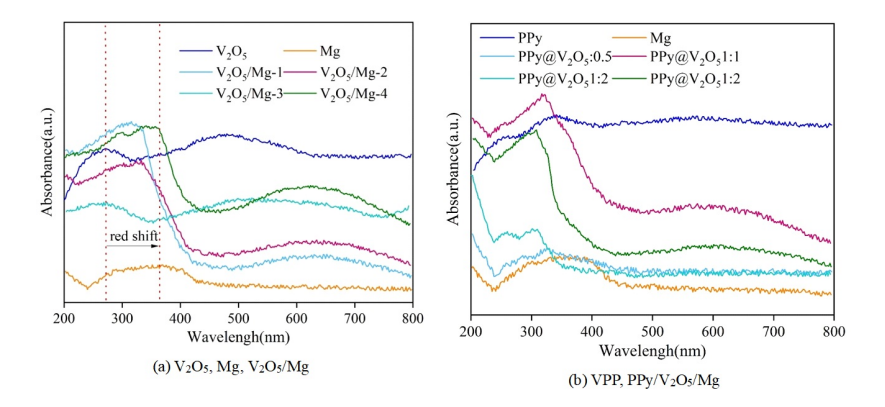


FIGURE 6 UV spectrum of the sample

3.4.4 | Scanning electron microscopy analysis of coatings

The SEM structure of the research sample is shown in Figure 7. (a) and (b) represent the cross-sectional microstructures after the experimental reaction. As seen in the figure, the pure Mg coating cross-section appears loose and striated. Poly(p-phenylenediamine) uniformly adheres to the surface of the layered VPP, undergoing an intercalation reaction. Furthermore, the uniform distribution of PPy within the coating effectively blocks the penetration of corrosive substances. This extends the diffusion pathways within the coating, thereby significantly enhancing its barrier properties.

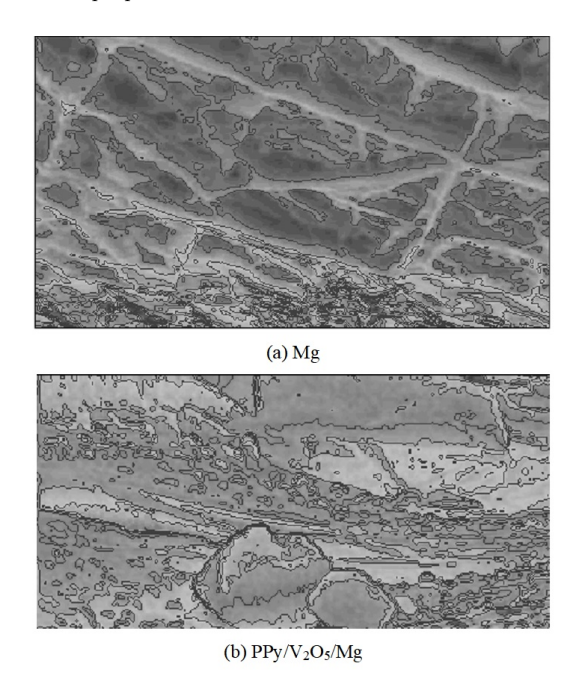


FIGURE 7 SEM image of the sample

3.5 | Corrosion resistance analysis

3.5.1 | Weightlessness testing

At temperatures of 30, 40, and 50° C, the corrosion inhibition efficiency of low-carbon steel is shown in Figure 8 when the PPy/V₂O₅/Mg concentrations are 0.2, 0.4, 0.6, 0.8, and 1.0 mmol/L, respectively. The concentration of the inhibitor significantly affects the corrosion inhibition efficiency. At constant temperatures, increasing concentrations of PPy/V₂O₅/Mg in hydrochloric acid solution enhance corrosion inhibition efficiency for low-carbon steel. Higher concentrations result in greater adsorption of PPy molecules onto the steel surface, reducing contact area between the steel and corrosive medium and thereby inhibiting corrosion reactions. At the same PPy/V₂O₅/Mg concentration, lower temperatures yield better corrosion inhibition performance for low-carbon steel. At higher temperatures, the adsorbed PPy/V₂O₅/Mg film on the low-carbon steel surface desorbs, increasing the contact area between the steel and the corrosive medium. Simultaneously, elevated temperatures accelerate the corrosion reaction rate, thereby reducing the corrosion inhibition efficiency of PPy/V₂O₅/Mg.

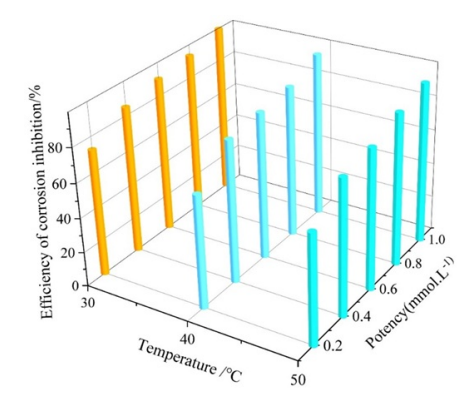


FIGURE 8 effect of temperature and concentration on corrosion inhibition efficiency

3.5.2 | Electrochemical testing

(1) Tafel Polarization Curves

Bare 316 stainless steel and 316 stainless steel electrodes electroplated with PAni, PAni/PPy, and $PAni/PPy - SiO_2$ μ m thick films were immersed in a 3.5% (mass fraction) NaCl solution. Tafel polarization curves were measured during the initial immersion phase, with results shown in Figure 9. Simultaneously, the influence of different SiO₂ contents in the films on their corrosion protection performance during the initial immersion stage was evaluated, with results shown in Figure 10. Table 3 lists the self-corrosion voltage (E_{corr}) and self-corrosion current (i_{corr}) obtained from the Tafel curves.

From the values of E_{corr} and i_{corr} in Table 3, it can be seen that after the PAni, PAni/PPy, and $PAni/PPy - SiO_2$ films were electrodeposited on the surface of 316 stainless steel, the E_{corr} was significantly improved compared to the bare steel, among which $PAni/PPy - SiO_2 > PAni/PPy > PAni$. The E_{corr} of the $PAni/PPy - SiO_2$ film is the highest and the i_{corr} is the smallest, indicating that the $PAni/PPy - SiO_2$

film has the best anti-corrosion performance. Due to the silanol shrinkage reaction during the film drying process, SiO2 forms a "silicon network structure", enhancing the density of the film. Moreover, because SiO_2 has good physical shielding properties, the permeability of water molecules on the $PAni/PPy-SiO_2$ composite film is lower. This enhances the mechanical shielding effect of the polymer film against corrosive media.

As shown in Table 3, within a certain range, the self-corrosion current in the composite film decreases initially and then increases as the SiO_2 content rises, while the self-corrosion voltage first increases and then decreases. When the molar ratio of aniline to nano- SiO_2 is 10:1, the film exhibits optimal anti-corrosion performance, with corresponding corrosion potentials and currents of 0.124 V and 3.215 \times 10⁻⁶ A/cm², respectively. This indicates that within a certain range, the anti-corrosion performance of the composite film enhances with increasing SiO_2 content. However, beyond a certain SiO_2 loading, the corrosion resistance of the composite film begins to decline. This occurs because excessive SiO_2 doping within the composite film leads to agglomeration on the metal surface, resulting in unevenly sized papillary particles. This affects the film's density, allowing the corrosive medium to penetrate the metal substrate surface and initiate corrosion reactions, thereby reducing the composite film's mechanical shielding effect against the corrosive medium.

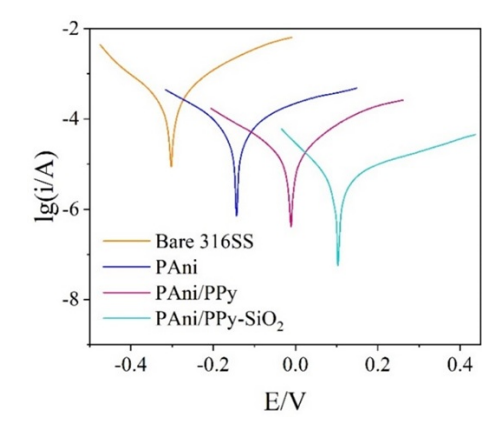


FIGURE 9 Initial tafel polarization curve

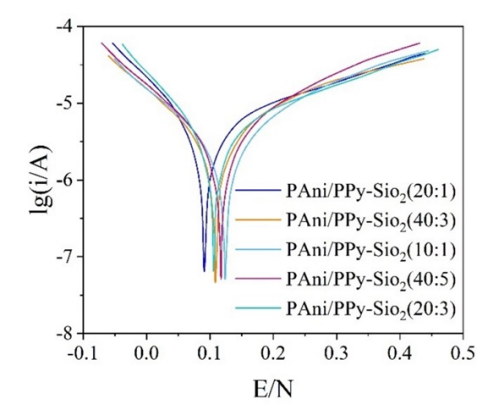


FIGURE 10 Initial tafel polarization curve

TABLE 3 E_{corr} and i_{corr} in accordance with Tafel curves of different membranes on 316SS

Membrane	E_{corr}/\mathbf{V}	$i_{corr}/(\mathbf{A}\cdot\mathbf{cm}^{-2})$
Bare 316SS	-0.36	2.831×10^{-4}
PAni/S1	-0.19	6.733×10^{-5}
PAni/PPy/S2	-0.05	1.893×10^{-5}
$PAni/PPy - SiO_2(20:1)/S3$	0.11	4.773×10^{-6}
$PAni/PPy - SiO_2(40:3)/S4$	0.109	3.552×10^{-6}
$PAni/PPy - SiO_2(10:1)/S5$	0.124	3.215×10^{-6}
$PAni/PPy - SiO_2(40:5)/S6$	0.117	3.144×10^{-6}
$PAni/PPy - SiO_2(20:3)/S7$	0.106	3.679×10^{-6}

(2) EIS Testing

Figure 11 shows the electrochemical impedance spectra (Nyquist plots) of bare 316 stainless steel and 316 stainless steel electrodes electroplated with PAni, PAni/PPy, and $PAni/PPy - SiO_2$ films, respectively, during the initial immersion in a 3.5% NaCl solution. Concurrently, the Nyquist plots of $PAni/PPy - SiO_2$ films with different nano- SiO_2 contents during the initial immersion phase were tested, as depicted in Figure 12.

Electrochemical impedance spectroscopy is an effective method for evaluating the corrosion resistance of thin films. A larger radius of the arc in the Nyquist plot indicates a higher film impedance value and stronger corrosion resistance. As shown in Figure 11, the order of corrosion resistance for the films is $PAni/PPy - SiO_2 > PAni/PPy > PAni$, all of which outperform bare steel. The $PAni/PPy - SiO_2$ composite film exhibits the largest arc radius, indicating that the addition of SiO_2 makes it more difficult for corrosive media (such as CI^-) to penetrate the film to the metal surface. As shown in Figure 12, the corrosion resistance of the films follows the order: $PAni/PPy - SiO_2$ (10:1) $PAni/PPy - SiO_2$ (40:5) $PAni/PPy - SiO_2$ (40:3) $PAni/PPy - SiO_2$ (20:1). This demonstrates that within a certain range, the corrosion resistance of the composite film increases with the addition of nano- SiO_2 . However, beyond a certain amount of SiO_2 , the corrosion resistance begins to decrease. This test result is consistent with the findings from the Tafel polarization curve tests.

Using Z-view software to perform circuit fitting on the EIS data from Figures 11 and 12 reveals two time constants in the impedance spectrum, though no macroscopic pores have yet formed on the thin film surface. The time constant in the high-frequency range stems from contributions of the film capacitance Cc and film resistance R_c , while the time constant in the low-frequency range originates from contributions of the film interface double-layer capacitance C_{dl} and film charge transfer resistance R_{ct} . Since the portion representing purely capacitive behavior deviates from pure capacitance during the electrode process, the pure capacitive element C is replaced by a constant phase element CPE, where n is the dispersion index. The fitted element parameters analyzed from Figures 8 and 9 are shown in Table 4. The table indicates that within a certain range, as the SiO₂ content in the composite film increases, both the film resistance and charge transfer resistance first increase and then decrease, while the film capacitance first decreases and then increases. This demonstrates that within a certain range, as the SiO₂ content increases, the corrosion resistance of the $PAni/PPy - SiO_2$ composite film first improves and then deteriorates.

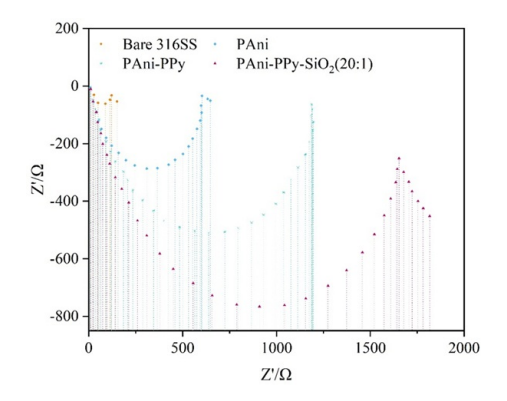


FIGURE 11 Initial electrochemical impedance spectrogram Nyquist curve

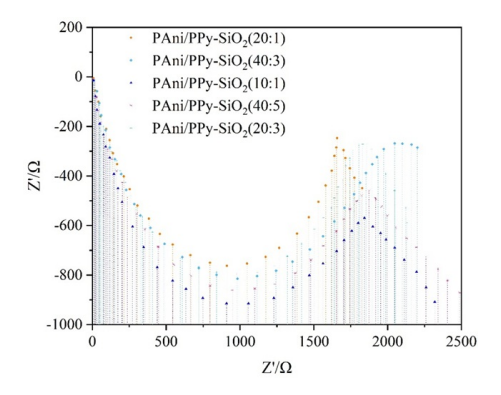


FIGURE 12 Nyquist curve

TABLE 4 EIS fitting parameters of different membranes on 316SS

Membrane	$R_s/(\Omega \cdot cm^2)$	$C_c/(F \cdot cm^{-2})$	n_1	$R_s/(\Omega \cdot cm^2)$	$C_{dl}/(F \cdot cm^2)$	n ₂	$R_{ct}/(\Omega \cdot cm^2)$
S1	8.33	4.3226E-4	0.78	139.3	0.00392	0.77	606.8
S2	9.36	2.9626E-4	0.82	171.5	0.00282	0.76	1032.5
S3	11.73	2.3134E-4	0.86	204.2	0.00209	0.83	1516.7
S4	11.35	1.7812E-4	0.87	246.17	0.00149	0.81	1781.6
S5	8.72	1.4622E-4	0.85	298.5	0.00106	0.86	1927.3
S6	7.67	1.5166E-4	0.88	265.3	0.00132	0.84	1844.6
S7	9.06	2.0407E-4	0.91	216.7	0.00175	0.85	1629.2

3.5.3 | Adsorption isotherms

To investigate the mechanism of corrosion inhibition by $PPy/V_2O_5/Mg$ on low-carbon steel in hydrochloric acid medium, Langmuir adsorption isotherm, Freundlich adsorption isotherm, and Frumkin adsorption isotherm

models were applied based on weight loss method experimental results.

The adsorption isotherm fitting results are shown in Figure 13. The Langmuir adsorption isotherm exhibited the closest linear correlation coefficient to 1, indicating that the adsorption behavior of $PPy/V_2O_5/Mg$ molecules on the low-carbon steel surface conforms to the Langmuir adsorption model.

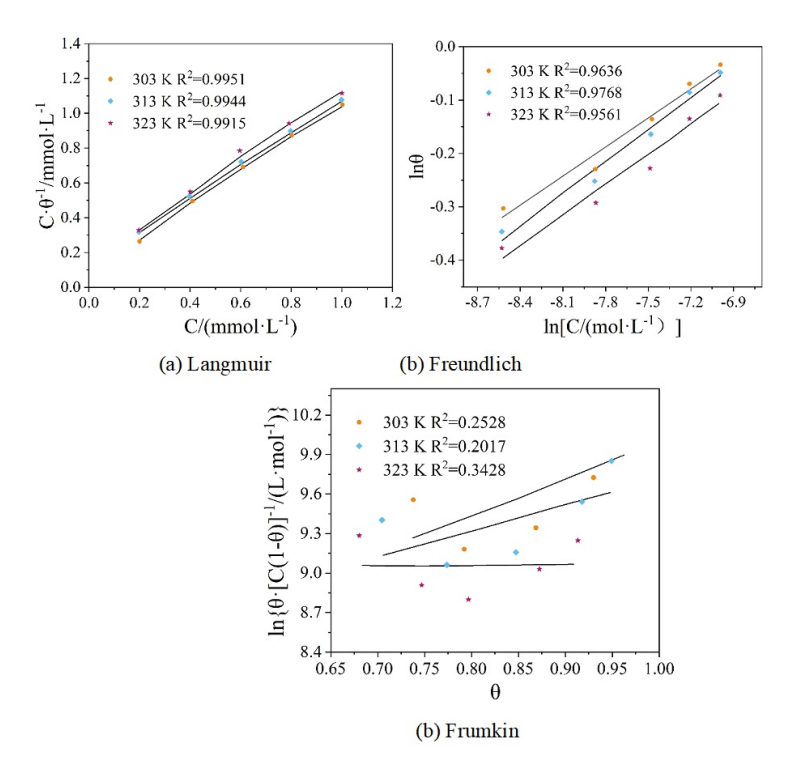


FIGURE 13 Fitting results of adsorption isotherms

Based on the Langmuir adsorption–isotherm fit, the thermodynamic parameters—the standard free energy of adsorption ΔG_{ads}° , the standard enthalpy of adsorption ΔH_{ads}° , and the standard entropy of adsorption ΔS_{ads}° —were obtained from

$$\Delta G_{ads}^{\circ} = -RT \ln(55.5 \, K_{ads}) \,, \tag{7}$$

$$\ln K_{ads} = -\frac{\Delta H_{ads}^{\circ}}{RT} + C,\tag{8}$$

$$\Delta G_{ads}^{\circ} = \Delta H_{ads}^{\circ} - T \, \Delta S_{ads}^{\circ}. \tag{9}$$

Here, R is the gas constant (8.314 J mol⁻¹ K⁻¹); T is the absolute temperature (K); K_{ads} is the adsorption equilibrium constant; 55.5 mol L⁻¹ is the molar concentration of water (included so that 55.5 K_{ads} is

dimensionless); and C is the integration constant.

The calculation results of thermodynamic parameters are listed in Table 5. The larger the K_{ads} value is, the more likely adsorption occurs, and the better the corrosion inhibition effect will be. Conversely, the corrosion inhibition effect is poor. As the temperature gradually rises, the K_{ads} value gradually decreases, indicating that the adsorption effect of PPy/V2O5/Mg molecules on the surface of low-carbon steel weakens at high temperatures. This might be because high-temperature conditions accelerate the thermal motion of molecules, causing PPy/V2O5/Mg molecules to desorb from the surface of low-carbon steel. A negative Δ Ga0ds value indicates that the PPy/V2O5/Mg molecules are spontaneously adsorbed on the surface of low-carbon steel. When $|\Delta G_{ads}^0| < 20 \text{kJ/mol}$, it indicates that the ads corrosion inhibitor molecules are adsorbed on the metal surface through electrostatic adsorption with the charged metal surface. When $|\Delta G_{ads}^0| > 40 \text{kJ/mol}$, the corrosion inhibitor molecules on the ADS surface and iron atoms undergo chemical adsorption through charge sharing or transfer. The PPy/V2O5/Mg molecules on the surface of low-carbon steel have a concentration of less than 20 kJ/mol and less than $|\Delta G_{ads}^0|$ kJ/mol, indicating that this adsorption process is the result of the interaction of two types of adsorption. The ΔH_{ads}^0 value is negative, indicating that the adsorption of PPy/V2O5/Mg molecules on the surface of low-carbon steel is an exothermic reaction, and the corrosion inhibition effect of low-carbon steel is affected by temperature changes.

1112 22 0 11abot poor viormou) name paramovers						
	T/K	$K_{ads}/(L \cdot mol^{-1})$	$\Delta G_{ads}^0/(kJ\cdot mol^{-1})$	$\Delta H_{ads}^0/(kJ\cdot mol^{-1})$	$\Delta S_{ads}^0/(k\cdot K^{-1}\cdot mol^{-1})$	
	303	9453	-33.28	-61.19	-89.71	
	313	8469	-34.05		-84.35	
	323	8162	-35.01		-79.29	

TABLE 5 Adsorption thermodynamic parameters

3.6 Wear resistance of composite coatings

Composite coating A consists of a 1mm-thick cured epoxy resin (D230:D2000 = 2:1) and a 1mm-thick polyurethane prepared with m(PTMG2000):m(polyether 3050) = 1:2. Using the same raw materials, an integrated coating B was formed with a 1mm-thick epoxy resin layer, a 0.5mm-thick polyurethane layer, and a 0.5mm-thick polyurea layer synthesized via slow reaction of polyetheramine P1000. Linear reciprocating friction tests were conducted on coatings A and B, with results shown in Figure 14. Figure 14(a) shows the variation in friction coefficient of Coatings A and B over reciprocating sliding friction time. Initially, the friction coefficients of both coatings increased with time before stabilizing. Due to the more polar urethane bonds in polyurethane molecules, which form additional hydrogen bonds with surrounding molecules, the coating becomes denser. Consequently, coating B exhibits a lower coefficient of friction than coating A during the stable phase. After 30 minutes of friction, coating B showed 3.78 mg less wear than coating A. The lower friction coefficient of coating B contributes to its reduced wear rate. The coating composed of epoxy resin E-51 primer cured at D230:D2000=2:1, polyurethane synthesized from PTMG2000:polyether 3050=1:2, and polyurea synthesized via slow reaction of polyetheramine P1000 exhibits excellent wear resistance.

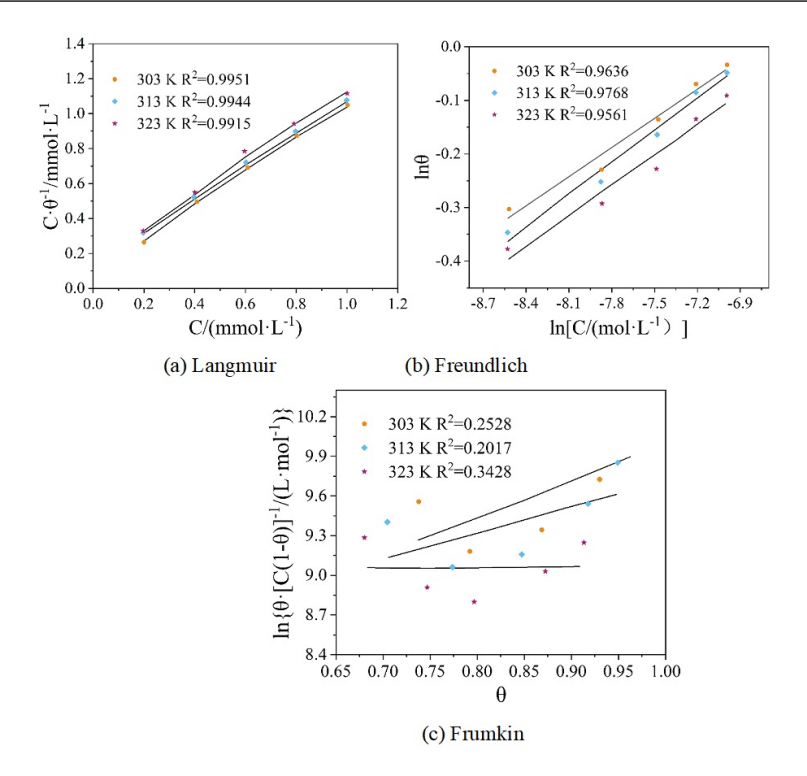


FIGURE 14 Comparative results of coating A and B after friction

4 | Conclusion

A novel VPP method for polymerizing PPy under mild conditions via V_2O_5 hydrocolloid was developed. Its anti-corrosion performance was investigated using gravimetric analysis, electrochemical testing, and isothermal adsorption models. The conclusions are as follows:

- (1) Compared to pure Mg, the addition of PPy/V_2O_5 enhanced Mg's mechanical properties, increasing tensile strength by 25.2% and decreasing elongation at break by 30%.
- (2) Excessive SiO₂ loading causes particle agglomeration on the metal surface, reducing film density and diminishing the composite film's protective capability for the metal substrate.
- (3) SEM, contact angle, and infrared spectroscopy analyses revealed that $PPy/V_2O_5/Mg$ adsorbed onto the low-carbon steel surface, forming a protective film that exerted a corrosion-inhibiting effect. The integrated coating system comprising the Mg/Si-10% intermediate protective layer provides more effective and durable protection for mechanical equipment.

References

- [1] Liang, S., Neisius, N. M., & Gaan, S. (2013). Recent developments in flame retardant polymeric coatings. *Progress in Organic Coatings*, 76(11), 1642-1665.
- [2] Smith, J. R., & Lamprou, D. A. (2014). Polymer coatings for biomedical applications: a review. Transactions of

- the IMF, 92(1), 9-19.
- [3] Gupta, H. S., Sethi, S. K., & Verma, A. (2023). Applications of coating materials: a critical overview. Coating Materials: Computational Aspects, Applications and Challenges, 81-109.
- [4] Aljibori, H. S., Alamiery, A., & Kadhum, A. A. H. (2023). Advances in corrosion protection coatings: A comprehensive review. *International Journal of Corrosion and Scale Inhibition*, 12(4), 1476-1520.
- [5] Caldona, E. B., Smith Jr, D. W., & Wipf, D. O. (2021). Surface electroanalytical approaches to organic polymeric coatings. *Polymer International*, 70(7), 927-937.
- [6] Zhang, P., Fan, H., Hu, K., Gu, Y., Chen, Y., Yan, J., ... & He, Y. (2018). Solvent-free two-component polyurethane conjugated with crosslinkable hydroxyl-functionalized ammonium polyphosphate: curing behaviors, flammability and mechanical properties. Progress in Organic Coatings, 120, 88-99.
- [7] Kapatel, P. M., & Patel, R. H. (2020). Green approach for the development of novel flame retardant waterborne polyurethanes: synthesis and its characterizations. *Materials Today: Proceedings*, 23, 389-399.
- [8] Shendi, H. K., Omrani, I., Ahmadi, A., Farhadian, A., Babanejad, N., & Nabid, M. R. (2017). Synthesis and characterization of a novel internal emulsifier derived from sunflower oil for the preparation of waterborne polyurethane and their application in coatings. *Progress in Organic Coatings*, 105, 303-309.
- [9] Xu, X., Jiang, Q., & Shi, Y. (2017, July). Analysis on the Major Environmental Factors Affecting the Weather Resistance of Polyester Coating. In *Chinese Materials Conference* (pp. 83-94). Singapore: Springer Singapore.
- [10] Thuy, N. T. B. (2017). Effects of additives, pigment and filler on physico-mechanical properties and weather resistance of polyurea coatings. Vietnam Journal of Science and Technology, 55 (5B), 153-153.
- [11] Rossi, S., Fedel, M., Petrolli, S., & Deflorian, F. (2016). Accelerated weathering and chemical resistance of polyurethane powder coatings. *Journal of Coatings Technology and Research*, 13(3), 427-437.
- [12] Silbert, S. D., Serum, E. M., LaScala, J., Sibi, M. P., & Webster, D. C. (2019). Biobased, nonisocyanate, 2K polyurethane coatings produced from polycarbamate and dialdehyde cross-linking. ACS Sustainable Chemistry & Engineering, 7(24), 19621-19630.
- [13] Zomorodian, A., Garcia, M. P., e Silva, T. M., Fernandes, J. C. S., Fernandes, M. H., & Montemor, M. F. (2013). Corrosion resistance of a composite polymeric coating applied on biodegradable AZ31 magnesium alloy. *Acta Biomaterialia*, 9(10), 8660-8670.
- [14] Potočić Matković, V. M., Čubrić, I. S., & Skenderi, Z. (2014). Thermal resistance of polyurethane-coated knitted fabrics before and after weathering. Textile Research Journal, 84(19), 2015-2025.
- [15] Kausar, A. (2018). Polymer coating technology for high performance applications: Fundamentals and advances. Journal of Macromolecular Science, Part A, 55(5), 440-448.
- [16] Ates, M. (2016). A review on conducting polymer coatings for corrosion protection. Journal of Adhesion Science and Technology, 30(14), 1510-1536.
- [17] Savill, T., & Jewell, E. (2021). Techniques for in situ monitoring the performance of organic coatings and their applicability to the pre-finished steel industry: A review. Sensors, 21(19), 6334.
- [18] Liu, L., Tan, E., Cai, Z. Q., Zhen, Y., & Yin, X. J. (2018, November). An integrated coating inspection system for marine and offshore corrosion management. In 2018 15th International Conference on Control, Automation, Robotics and Vision (ICARCV) (pp. 1531-1536). IEEE.
- [19] Kanemitsu, T., & Takaya, S. (2023). Applicability of AC impedance method for measuring time-variant corrosion rate to cracked and crack-repaired reinforced concrete. *Materials and Structures*, 56(1), 20.